Electronic Supplementary Information for

Ultra-thick Graphene Bulk Electrodes of Supercapacitors for Compact Energy Storage

Huan Li, Ying Tao, Xiaoyu Zheng, Jiayan Luo*, Feiyu Kang, Hui-Ming Cheng and Quan-Hong Yang*

*Corresponding authors. E-mail: qhyangcn@tju.edu.cn; jluo@tju.edu.cn

This file includes:

Figure S1-S13

Table S1-S4

References

Table of contents

1. **Figure S1:** Porosity characterization of rGOM monoliths heated at different temperatures.
2. **Figure S2:** Pore size distributions of PaGM.
3. **Figure S3:** Mechanistic study of the porosity tuning process.
4. **Figure S4:** XPS patterns of rGOM, rGOM-600, PaGM.
5. **Figure S5:** Raman spectra of rGOM-600, PaGM-$ZnCl_2$, GM-KOH.
6. **Figure S6:** TGA curve of rGOM monolith.
7. **Figure S7:** TGA curves of rGOM/Zn^{2+} and Cl^- containing salts mixtures.
8. **Figure S8:** Preparation of supercapacitor electrodes.
9. **Figure S9:** Relationship between $ZnCl_2$/rGOM mass ratio and BET surface area as well as porosity.
10. **Figure S10:** Rate performance and operation voltage investigation for 400 μm thick electrode.
11. **Figure S11:** Rate performance and cyclic stability of pellet electrodes with different thickness.
12. **Figure S12:** Charge-discharge curves of a combining device with series or parallels.
13. **Figure S13:** Electrochemical performance of graphene pellets electrodes in 6 M KOH electrolyte
14. **Table S1:** BET surface area and resulting form of the products interfered by several Zn^{2+} and Cl^- containing salts
15. **Table S2:** Details for determining tortuosity.
16. **Table S3:** Performance of reported electrode materials for symmetric supercapacitors.
17. **Table S4:** Performance of reported electrode materials for asymmetric supercapacitors.
18. **References.**

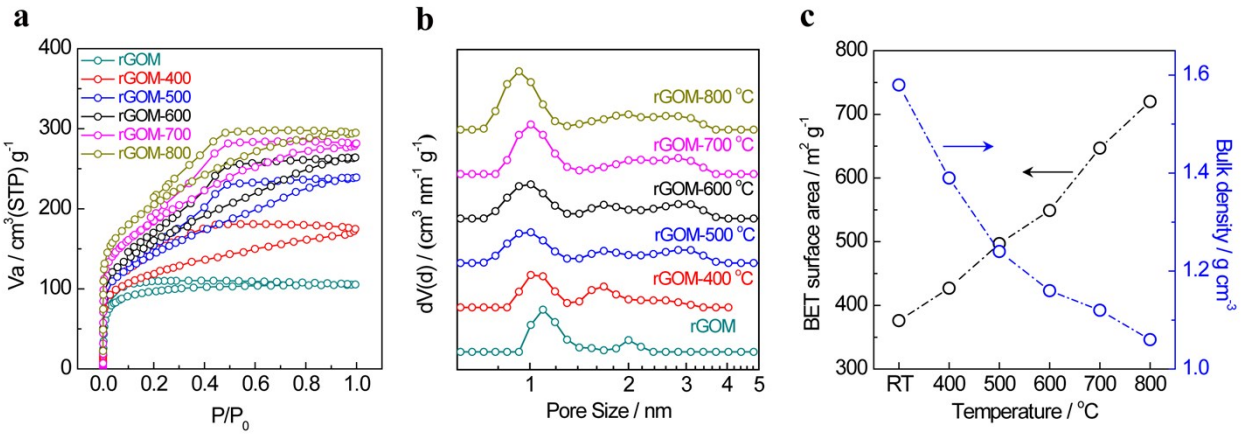

Figure S1 Porosity characterization of rGOM monoliths heated at different temperatures. N_2 adsorption-desorption isotherms (a) and pore size distributions (b) of rGOM monoliths heated at different temperatures. It shows the increased surface area and decreased density after heat treatment (c).

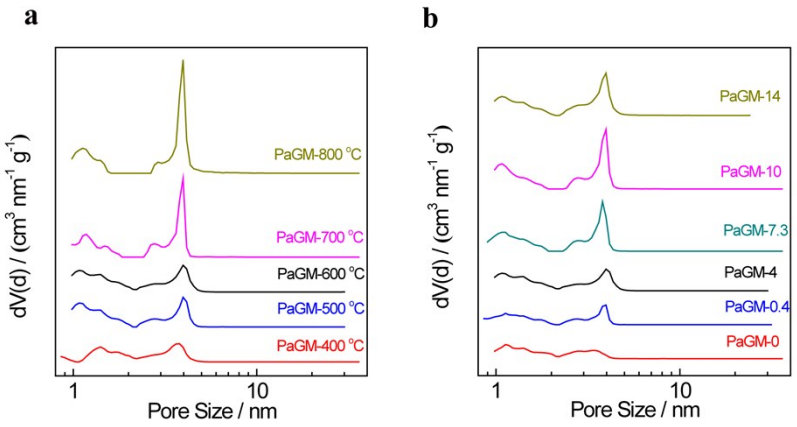

Figure S2 Pore size distributions of PaGM. PaGM products heat treated from 400 °C to 800 °C (a) and PaGM products with mass ratio ranging from 0.8~14 at 600 °C (b).

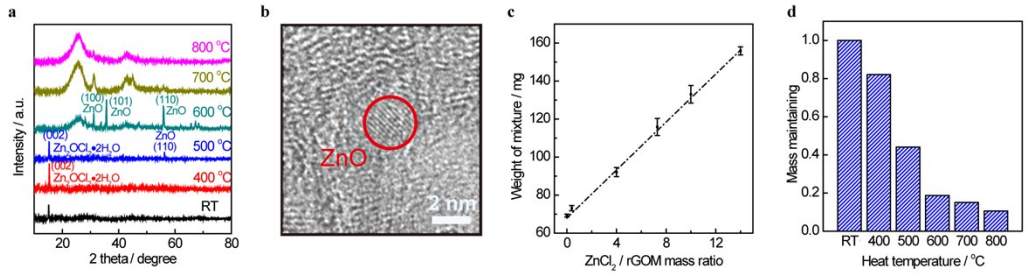

Figure S3 Mechanistic study of the porosity tuning process. (a) XRD patterns of a $ZnCl_2$/rGOM mixture heated at different temperatures before washing showing hydrolysis products present in the mixture. (b) TEM image of a rGOM/$ZnCl_2$ mixture after 600 °C heat treatment. (c) Mass retention of 600 °C heated mixture before acid washing. Remaining of $Zn_2OCl_2{\cdot}2H_2O$ and ZnO in the graphene monoliths is highly dependent on the $ZnCl_2$/rGOM mass ratio. (d) Mass retention of mixture heated at different temperatures before acid washing. The evaporation of $ZnCl_2$ results in the mass reduction before 600 °C and the continuous mass reduction at 700 and 800 °C can be attributed to the carbon thermal reaction between ZnO and graphene.

The range of heating temperatures needs to be well controlled. To identify effect of $ZnCl_2$ on rGOM during the pore-forming process, $ZnCl_2$/rGOM monoliths treated at different temperatures before washing Zn^{2+} containing salts were analyzed by X-ray diffraction (XRD) (Figure S3a). Zinc oxide chloride hydrate ($Zn_2OCl_2{\bullet}2H_2O$) was observed in the mixture before heating, which can readily crystallize from an aqueous solution during the mixture preparation step for the hygroscopic nature of $ZnCl_2$ (Eq.1).

$$ZnCl_2 + H_2O \rightarrow Zn_2OCl_2{\bullet}2H_2O \quad (1)$$

ZnO starts to emerge at 500 °C and dominants at 600 °C in the mixture produced by the decomposition of $Zn_2OCl_2{\bullet}2H_2O$ (Eq.2).

$$Zn_2OCl_2{\bullet}2H_2O \rightarrow ZnO + ZnCl_2 + H_2 \quad (2)$$

The presence of ZnO nanoparticles is also confirmed by transmission electron microscopy (TEM) observations (Figure S3b), and these nanoparticles need to be washed by an acidic solution. It is noted that the amount of ZnO in the graphene monoliths is highly dependent on the $ZnCl_2$/rGOM mass ratio, as is evident from the higher weight of ZnO in heated products before acid washing from the $ZnCl_2$/rGOM mixture with higher mass ratios (Figure S3c). This also helps explain the positive correlation between the amount of $ZnCl_2$ and the porosity and surface area of the graphene monoliths. The $ZnCl_2$ and its hydrolysis residue ZnO have made pores in the monoliths after evaporation and washing. When the heating temperature was further increased, the peak intensity of ZnO diminished, suggesting occurrence of the carbon thermal reaction between ZnO and the graphene sheets (Eq.3).

$$ZnO + C \rightarrow Zn + CO_x \quad (3)$$

The resulting Zn metal needs to be washed by diluted acid solution for pore formation. Besides, significant mass loss of the ZnO/graphene mixture was observed at temperature higher than 600 °C (Figure S3d), which could only be explained by the reactive mutual consumption between ZnO and graphene as detailed above. This severe etching also reduced the mechanical strength of the treated samples at 700 °C and 800 °C.

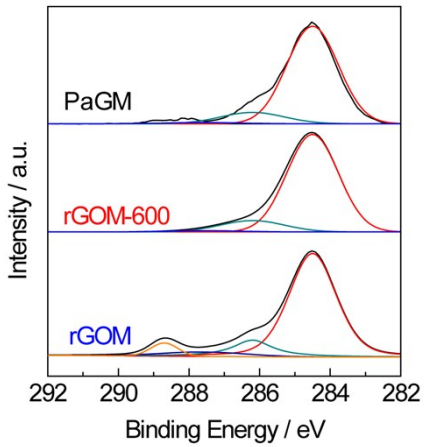

Figure S4 XPS patterns (C1s) of rGOM, rGOM-600, PaGM. No obvious difference of PaGM and rGO-600 shows that $ZnCl_2$ does not alter the graphene monolith's chemical properties.

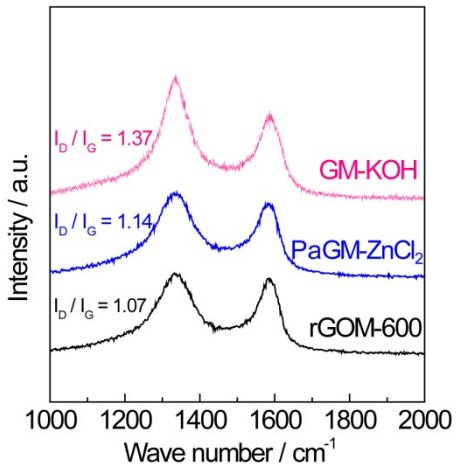

Figure S5 Raman spectra of rGOM-600, PaGM-$ZnCl_2$, GM-KOH. The increased I_D/I_G of GM-KOH shows different mechanism of KOH and $ZnCl_2$ for the pore evolution on graphene monoliths.

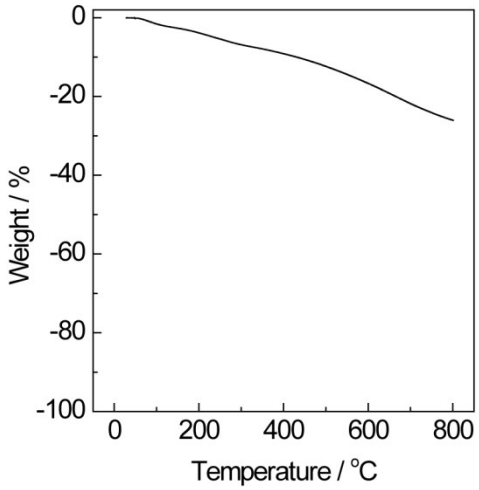

Figure S6 TGA curve of rGOM monolith. The weight retention of rGOM monolith at 600 °C is ~83 %.

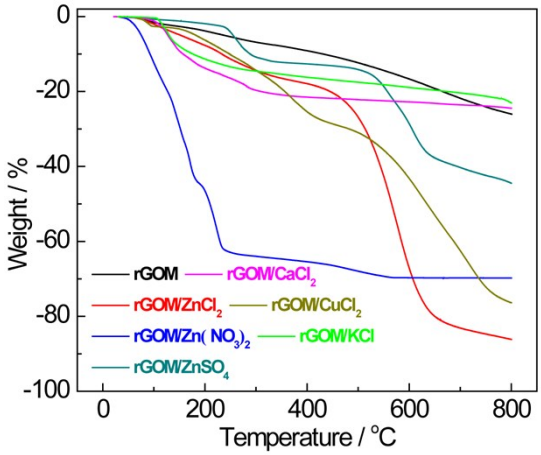

Figure S7 TGA curves of rGOM/Zn^{2+} and Cl^- containing salts mixtures. The weight loss is related to the boiling point and decomposition of the salts.

Table S1 BET surface area and resulting form of the products interfered by several Zn^{2+} and Cl^- containing salts

	Boiling point /°C	BET surface area / $m^2\ g^{-1}$	Resulting form	Digital pictures
rGOM-600	N/A	549	Bulk form	
$ZnCl_2$	732	891	Bulk form	
$Zn(NO_3)_2$	125	551	Pulverized	
$ZnSO_4$	500	550	Pulverized	
$CaCl_2$	1600	568	Pulverized	
$CuCl_2$	933	728	Pulverized	
KCl	1420	439	Pulverized	

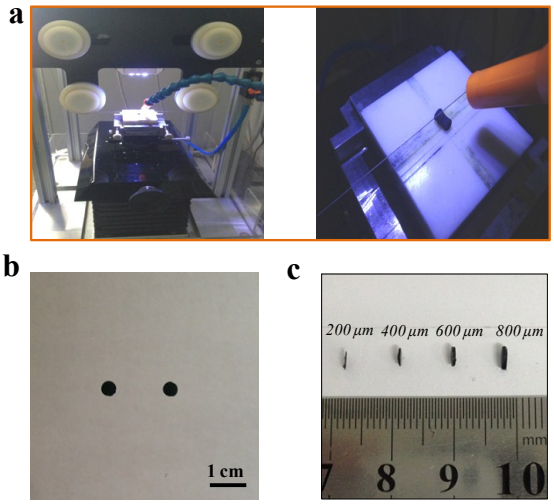

Figure S8 Preparation of supercapacitor electrodes. (a) Slicing Process of PaGM electrodes for supercapacitor. (b) Photo of electrodes in front view. (c) Comparison of electrodes with different thickness in cross section.

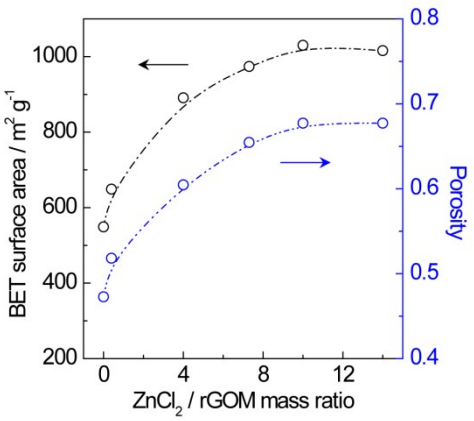

Figure S9 Relationship between $ZnCl_2$/rGOM mass ratio and BET surface area as well as porosity. BET surface area and porosity can be tuned by simply altering $ZnCl_2$/rGOM mass ratio.

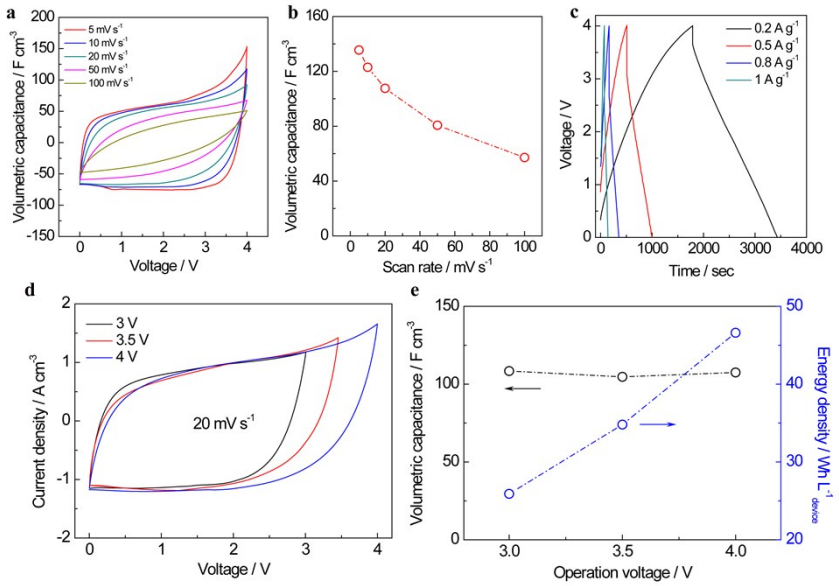

Figure S10 Rate performance and operation voltage investigation for 400 μm thick electrode. (a) CV curves of graphene pellet electrode from 5 mV s^{-1} to 100 mV s^{-1}; (b) Rate performance; (c) Charge-discharge curves, the IR drop is 0.33 V, 0.84 V, 1.34 V at 0.2 A g^{-1}, 0.5 A g^{-1}, 0.8 A g^{-1}, respectively. (d) CV curves of devices working in different operation voltage; (e) Relationship between operation voltage and volumetric capacitance as well as volumetric energy density. The electrode shows similar capacitance while the energy density reaches the highest from 0 V to 4 V.

The CV curves show quasi-rectangular shape at low scan rate but show slightly distortion at high scan rate mainly due to polarization (Figure S10a). The volumetric capacitance is 136 F cm^{-3} at 5 mV s^{-1} and maintains 57 F cm^{-3} at 100 mV s^{-1} even with such an ultra-thick electrode (Figure S10b).

The charge-discharge curves show quasi-symmetric shape from 0.2 A g^{-1} to 1 A g^{-1} that indicate an outstanding capacitive behavior (Figure S10c). The IR drop at 0.2 A g^{-1}, 0.5 A g^{-1} and 0.8 A g^{-1} are 0.33 V, 0.84 V, 1.34 V respectively. High IR drop can be mainly attributed to ultra-high electrode thickness.

To investigate the performance of electrodes with different voltage ranges, we carried out CV tests o such graphene pellet electrode in ionic liquid electrolyte with the range of 0~3 V, 0~3.5 V and 0~4 V. Quasi-rectangular shapes are observed in these operation voltage ranges, indicating excellent capacitive behavior of such electrodes. The electrodes show similar volumetric capacitance (108.4 F cm^{-3}, 104.7 F cm^{-3}, 107.5 F cm^{-3} at 20 mV s^{-1}) with the range of 0~3 V, 0~3.5 V and 0~4 V (Figure S10d). However, the corresponding volumetric energy density is 25.9 Wh L^{-1}, 34.8 Wh L^{-1}, 46.6 Wh L^{-1}, respectively ($E_v=0.125C_vU^2f/3.6$) (Figure S10e). In order to achieve high volumetric energy density, the operation voltage is chosen at 0~4 V, which is suitable for neat ionic liquid.[1]

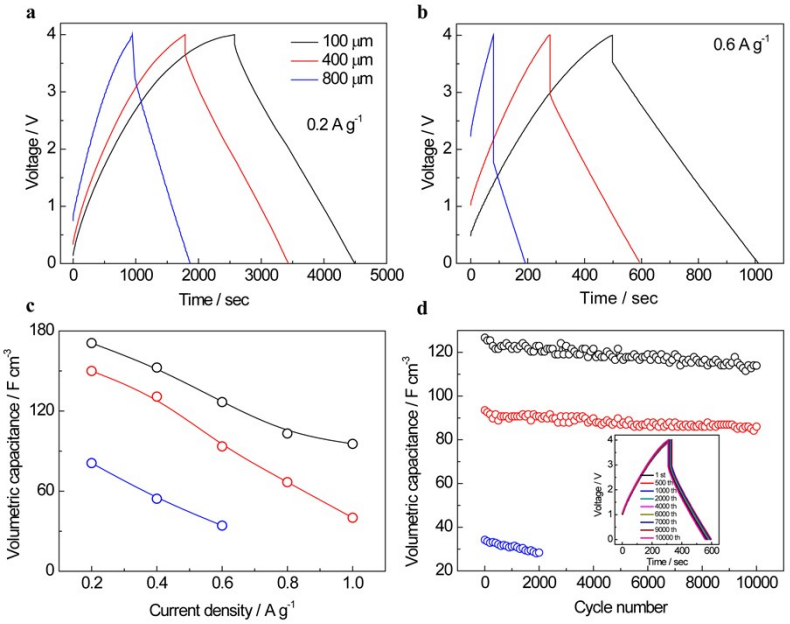

Figure S11 Rate performance and cyclic stability of pellet electrodes with different thickness. Charge-discharge curves CV at 0.2 A g^{-1} (a) and 0.6 A g^{-1} (b) with the electrodes thickness of 100 μm, 400 μm and 800 μm. The IR drops are 0.15 V, 0.33 V, 0.72 V for 100 μm, 400 μm, 800 μm thick electrodes at 0.2 A g^{-1} and the voltage drop have an obvious increase at 0.6 A g^{-1} for such electrodes. (c) Rate performance and of 100 μm, 400 μm and 800 μm thick electrodes; (d) cyclic stability of such electrodes with different thickness at 0.6 A g^{-1}. The inset shows the charge-discharge curves of 400 μm thick electrode and the capacitance retention is up to 90 % after 10000 cycles.

Table S2 Details for determining tortuosity

Porosity (ε)	κ / S m^{-1}	$R_\infty \cdot A$	L_j / μm	$\sum L_j$ / μm	Tortuosity (τ)
0.473	0.456	57.523±1.48	400	800	1.55±0.04
0.518	0.456	46.384±1.69	400	800	1.37±0.05
0.605	0.456	35.114±0.58	400	800	1.21±0.02
0.655	0.456	29.751±0.80	400	800	1.11±0.03
0.677	0.456	27.198±1.29	400	800	1.05±0.05
0.605	0.456	7.681±0.22	100	200	1.06±0.03
0.605	0.456	16.490±0.44	200	400	1.14±0.03
0.605	0.456	26.563±1.31	300	600	1.27±0.06
0.605	0.456	36.410±1.16	400	800	1.25±0.04
0.605	0.456	63.433±1.74	600	1200	1.45±0.04
0.605	0.456	95.956±1.74	800	1600	1.64±0.03

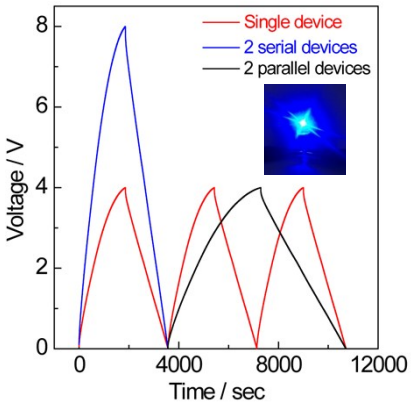

Figure S12 Charge-discharge curves of a combining device with series or parallels. A single device is shown for comparison. The inset LED is lightened by the tandem device. The device performance without much loss can meet the scalable high current and voltage applications.

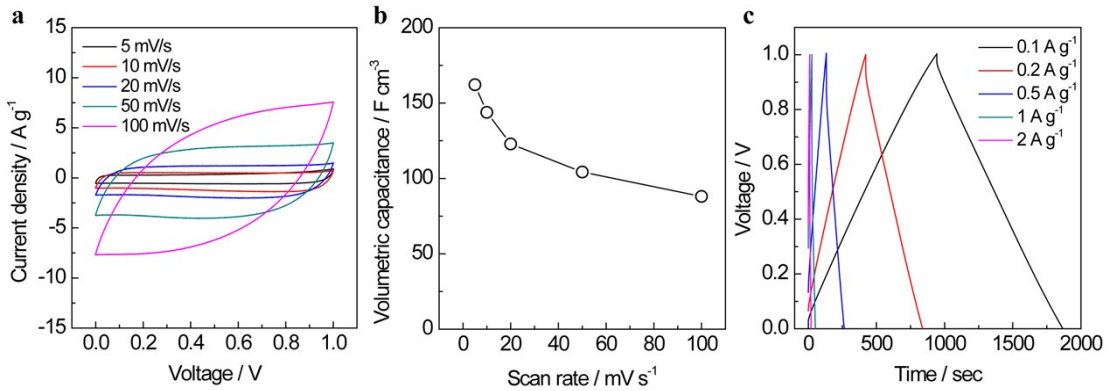

Figure S13 Electrochemical performance of graphene pellets electrodes in 6 M KOH aqueous electrolyte. (a) CV curves, (b) Capacitance retention and (c) Charge-discharge curves. The volumetric capacitance is 162 F cm^{-3} at 5 mV s^{-1} for the 400 micrometers thick electrode and volumetric energy density of 4.4 Wh L^{-1} at a power density of 79.2 W L^{-1} can be achieved .

Table S3 Performance of reported electrode materials for symmetric supercapacitors

Materials reported	**Electrolyte Operating voltage [V]**	**C_g [F g^{-1}]**	**C_v [F cm^{-3}]**	**Electrode Thickness µm**	***f***	**E_{vol} [Wh L^{-1}]**	**Ref.**
PaGM	$BMIMBF_4$ 4 V	172.4 151.0 120.9	150.0 131.4 105.2	***400*** ***500*** ***600***	***0.78*** ***0.81*** ***0.84***	64.7 (device) 59.3 (device) 49.0 (device)	This work
EM-CCG	$EMIMBF_4$/AN 3.5 V	167.1	208.9	***80***	***~0.54***	59.9 (device)	2
HGF	$EMIMBF_4$/AN 3.5 V	298	212	***140***	***0.62***	49.2 (device)	3
LSG	$TEABF_4$/AN 3 V	276	13.2	***7.6***	***0.19***	1.36 (device)	4
aMP	MPPyTFSI 4 V	189	94.5	***40***	***0.38***	19 (device)	5
Carbon fiber	PVA/H_3PO_4 1 V	510.8 ±34.4	300	***50***	***~0.6***	~6.3 (device)	6
Ac-Gr/SWCNT	$EMIMBF_4$ 4 V	199	211	***N/A***	***N/A***	117.2 (two-electrode)	7
1T MoS_2	$EMIMBF_4$/MECN 3.5 V	~50	250	***5***	***N/A***	110 (two-electrode)	8
r[GO-CNT]	$TEABF_4$/PC 3 V	109.7	165	***1~3***	***N/A***	51.4 (two-electrode)	9
Compressed a-MEGO	$TEABF_4$/AN 3.5 V	147	110	***57***	***N/A***	48 (two-electrode)	10
Ti_3C_2 Clay	H_2SO_4 1 V	245	900	***5***	***N/A***	37.8 (two-electrode)	11
HPGM	$TEABF_4$/AN 2.5 V	110	174	***N/A***	***N/A***	37.6 (two-electrode)	12
Curved graphene	$EMIMBF_4$ 4 V	154	46.2	***N/A***	***N/A***	25.7 (two-electrode)	1
a-MEGO	$BMIMBF_4$/AN 3.5 V	165	59.4	***40~50***	***N/A***	25.3 (two-electrode)	13
Ti_3C_2 Paper	KOH 1.1 V	~130	340	***2~20***	***N/A***	14.28 (two-electrode)	14

Table S4 Performance of reported electrode materials for asymmetric supercapacitors.

Materials reported	Electrolyte Operating voltage [V]	Electrode Thickness μm	*f*	E_{vol} [Wh L^{-1}]	Ref.
PaGM	$BMIMBF_4$ 0 V-4 V	***400*** ***500*** ***600***	***0.78*** ***0.81*** ***0.84***	64.7 (device) 59.3 (device) 49.0 (device)	This work
Graphite//AC	$LiPF_6$ in EC/DMC 1.5 V-4.5 V	***N/A***	***N/A***	111.8 (two-electrode)	15
C-LTO//AC	$LiPF_6$ in PC 1.5 V-2.5 V	***30***	***N/A***	57 (two-electrode)	16
CNTs//$Li_4Ti_5O_{12}$	$LiPF_6$ in EC/DEC 0 V-3 V	***N/A***	***N/A***	4.38 (device)	17
$NiCo_2O_4$/graphene// HFAC	KOH 0 V-1.55 V	***N/A***	***N/A***	76.3 (two-electrode)	18
nc- $Li_4Ti_5O_{12}$//CNF	$TEABF_4$/PC 1.5 V-3 V	***60***	***N/A***	40 (two-electrode)	19
GNiF//GTF	PVA/KOH 0 V-1.7 V	***6//7.4***	***N/A***	23.5 (two-electrode)	20

References and Notes:

1. C. Liu, Z. Yu, D. Neff, A. Zhamu and B. Z. Jang, *Nano letters*, 2010, **10**, 4863-4868.
2. X. Yang, C. Cheng, Y. Wang, L. Qiu and D. Li, *Science*, 2013, **341**, 534-537.
3. Y. Xu, Z. Lin, X. Zhong, X. Huang, N. O. Weiss, Y. Huang and X. Duan, *Nature communications*, 2014, **5**, 4554.
4. M. F. El-Kady, V. Strong, S. Dubin and R. B. Kaner, *Science*, 2012, **335**, 1326-1330.
5. H.-C. Huang, C.-W. Huang, C.-T. Hsieh and H. Teng, *Journal of Materials Chemistry A*, 2014, **2**, 14963.
6. D. Yu, K. Goh, H. Wang, L. Wei, W. Jiang, Q. Zhang, L. Dai and Y. Chen, *Nature Nanotechnology*, 2014, **9**, 555-562.
7. P. Duy Tho, T. H. Lee, D. H. Luong, F. Yao, A. Ghosh, L. Viet Thong, T. H. Kim, B. Li, J. Chang and Y. H. Lee, *ACS Nano*, 2015, **9**, 2018-2027.
8. M. Acerce, D. Voiry and M. Chhowalla, *Nature Nanotechnology*, 2015, **10**, 313-318.
9. N. Jung, S. Kwon, D. Lee, D. M. Yoon, Y. M. Park, A. Benayad, J. Y. Choi and J. S. Park, *Advanced Materials*, 2013, **25**, 6854-6858.
10. S. Murali, N. Quarles, L. L. Zhang, J. R. Potts, Z. Tan, Y. Lu, Y. Zhu and R. S. Ruoff, *Nano Energy*, 2013, **2**, 764-768.
11. M. Ghidiu, M. R. Lukatskaya, M. Q. Zhao, Y. Gogotsi and M. W. Barsoum, *Nature*, 2014, **516**, 78-81.
12. Y. Tao, X. Xie, W. Lv, D. M. Tang, D. Kong, Z. Huang, H. Nishihara, T. Ishii, B. Li, D. Golberg, F. Kang,

T. Kyotani and Q. H. Yang, *Scientific Reports*, 2013, **3**, 2975.

13. Y. Zhu, S. Murali, M. D. Stoller, K. J. Ganesh, W. Cai, P. J. Ferreira, A. Pirkle, R. M. Wallace, K. A. Cychosz, M. Thommes, D. Su, E. A. Stach and R. S. Ruoff, *Science*, 2011, **332**, 1537-1541.

14. M. R. Lukatskaya, O. Mashtalir, C. E. Ren, Y. Dall'Agnese, P. Rozier, P. L. Taberna, M. Naguib, P. Simon, M. W. Barsoum and Y. Gogotsi, *Science*, 2013, **341**, 1502-1505.

15. V. Khomenko, E. Raymundo-Pinero and F. Beguin, *Journal of Power Sources*, 2008, **177**, 643-651.

16. H.-G. Jung, N. Venugopal, B. Scrosati and Y.-K. Sun, *Journal of Power Sources*, 2013, **221**, 266-271.

17. W. H. Zuo, C. Wang, Y. Y. Li and J. P. Liu, *Scientific Reports*, 2015, **5**.

18. Z. Li, Z. W. Xu, H. L. Wang, J. Ding, B. Zahiri, C. M. B. Holt, X. H. Tan and D. Mitlin, *Energy & Environmental Science*, 2014, **7**, 1708-1718.

19. K. Naoi, S. Ishimoto, Y. Isobe and S. Aoyagi, *Journal of Power Sources*, 2010, **195**, 6250-6254.

20. M. Li, Z. Tang, M. Leng and J. M. Xue, *Advanced Functional Materials*, 2014, **24**, 7495-7502.